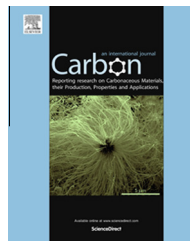




ELSEVIER

Available at www.sciencedirect.com**ScienceDirect**journal homepage: www.elsevier.com/locate/carbon

Growth of carbon dendrites on cathode above liquid ethanol using surface plasma

Dmytro Kozak ^{*}, Etsuro Shibata, Atsushi Iizuka, Takashi Nakamura

Institute of Multidisciplinary Research for Advanced Materials (IMRAM), Tohoku University, 1, 1 Katahira, 2-Chome, Aobaku, Sendai 980-8577, Japan

ARTICLE INFO

Article history:

Received 6 November 2013

Accepted 27 December 2013

Available online 4 January 2014

ABSTRACT

The newly developed method presented in this paper allows growth of carbon dendrites, which exhibit glassy carbon- and pyrocarbon-like structures, using surface plasma on the cathode surface above dehydrated ethanol. The process is based on the polarization of polar organic molecules under the influence of external high electric field strength. Ethanol molecules have a dipole moment, they were aligned in the direction of the electric field, and the process of electronic/dipole-relaxation polarization started to occur in liquid ethanol. The dipole density was maximized in the cathode region located at 7–10 mm above the liquid ethanol owing to the non-uniform electric field. The electronic breakdown started in the region experiencing the maximum electric field strength. The decomposition of ethanol molecules changed the condition of the gas phase in the breakdown region a resultant current started to flow in the circuit. The growth of carbon dendrites on the Pt cathode, possible under the stability of surface plasma discharges, was characterized by formation of carbon nuclei on the cathode surface. Another advantage of the plasma surface process is that it enables growth of carbon dendrite on dielectric surfaces without increasing of plasma power generation.

© 2014 Elsevier Ltd. All rights reserved.

1. Introduction

Carbon nanomaterials offer a wide range of useful properties including electrical conductance, thermal resistance, and exceptional strength, making them interesting materials to a broad range of industries. There are a wide variety of variety carbon nanostructures; however, they all have some things in common. These materials are predominantly composed of pure carbon, they are carbon allotropes. Carbon nanomaterial's range from well-known allotropes of diamond, graphite to fullerenes, graphene, and more complex structures such as carbon nanotubes, pyrocarbon and glassy carbon.

The popular synthesis methods for carbon materials include arc discharge, laser ablation, plasma torch, chemical vapor deposition (CVD) and sonochemistry. Depending on

the materials being synthesized, these methods each have both positive and negative aspects, prompting researchers to find new synthesis techniques for carbon nanomaterials.

Using a solution of water and carbon-containing liquids a plasma process was applied for synthesizing of nanodiamonds [1,2]. The solution was negatively biased via a graphite block immersed in the solution. The initial conductivity of the solution was adjusted to about 0.02 S/m by adding a small amount of potassium acetate. The deposition was carried out for 30 min at different temperatures 900 °C, 1000 °C and 1100 °C [1]. The water-methanol system had the highest diamond forming ability [2]. However, the mixtures of water with 1-propanol, 2-propanol and glycerol showed no evidence of diamond formation and the growth of long dendrites often disturbed the plasma discharge [2]. Furthermore,

^{*} Corresponding author.

E-mail address: dm.s.kozak@gmail.com (D. Kozak).

direct-current glow-discharge CVD was used to deposit of nanocrystalline carbon films on a pristine silicon substrate without any surface pretreatment [3]. A methane–hydrogen mixture was utilized for the synthesis of nanocrystalline carbon films at substrate temperatures of 800 °C, 880 °C and 950 °C for 8 h.

Heiman et al. [3,4] showed the importance of the hydrogen adsorption/desorption processes in the nucleation and growth of nanocrystalline diamond films deposited by direct current glow discharge within the narrow temperature range of 880 ± 10 °C. Carbon aerosols with pyrocarbon-like structure were produced by non-thermal plasma-assisted decomposition of methane at atmospheric pressure between temperatures 850 °C and 900 °C [5]. The synthesis of carbon structures, such as carbon nanoflakes [6], vertically oriented graphene sheets [7] and carbon nanowalls [8,9] was performed at atmospheric pressure using microwave plasma-enhanced CVD in gaseous carbon-bearing mediums.

Liquid–gas interfacial plasma was applied in the fabrication of metal nanoparticles [10–14]. Electrically conductive liquids, such as ionic liquids and electrolyte solutions were used for these experiments. These solutions easily dissociated into ions allowing the passage of an electric current in the circuit and the formation of metal nanoparticles during the plasma process.

In this paper, we report the growth of carbon dendrite with glassy carbon- and pyrocarbon-like structures using surface plasma at room temperature and near-ambient pressure with dehydrated polar liquid ethanol (C_2H_5OH) as the carbon precursor. This process is based on the polarization of the organic molecules under the influence of external high electric field strength to conduct an electric current. Because ethanol molecules have a dipole moment, they began to align with the direction of the electric field, and the process of electronic/dipole-relaxation polarization process started to

occur in the liquid ethanol. The electronic breakdown occurred between the Pt-cathode and the surface liquid ethanol where the dipole density reached a maximum due to non-uniform electric field strength.

2. Experimental setup

Fig. 1(a) shows the general scheme of the experimental setup. Two 0.3 mm in diameter Pt-electrodes (99.9% purity, Nilaco) were protected by quartz tubes. The electrode-anode was immersed in 30 ml of liquid ethanol (Super Dehydrated (99.5%), Wako). Another electrode-cathode was placed at 7–10 mm distance above the ethanol surface. A protective Ar gas atmosphere was added to the glass vessel with at gas flow rate of 250 ml/min (**Fig. 1(a)**). The surface plasma was generated using a high voltage DC power supply with the pulsating frequency about 33 kHz. The power voltage and current of power supply were adjusted in the range of 0.6–1.1 kV and 220–273 mA, respectively. At the beginning of the surface plasma process, the liquid ethanol temperature was about 20 °C. When the hot-spot formed during the carbon dendrite growth, the temperature of liquid ethanol did not exceed 55–60 °C (**Fig. 1(b)**).

The temperature of hot-spot was estimated to be approximately 1000 °C through a visual comparison of the scale surface of the heated metal. The carbon dendrite growth continued until the cathode touched the liquid ethanol surface. The cathode was raised an additional 5–10 mm above the surface, and the growth continued again (**Fig. 1(b)**). The total duration of the carbon dendrite growth was approximately 2 h.

The surface morphology of the as-prepared carbon dendrite was observed by optical microscope (Keyence VH-Z100R) and scanning electron microscope (SEM, Hitachi SU8000), field emission SEM (FE-SEM, Hitachi S4800). A

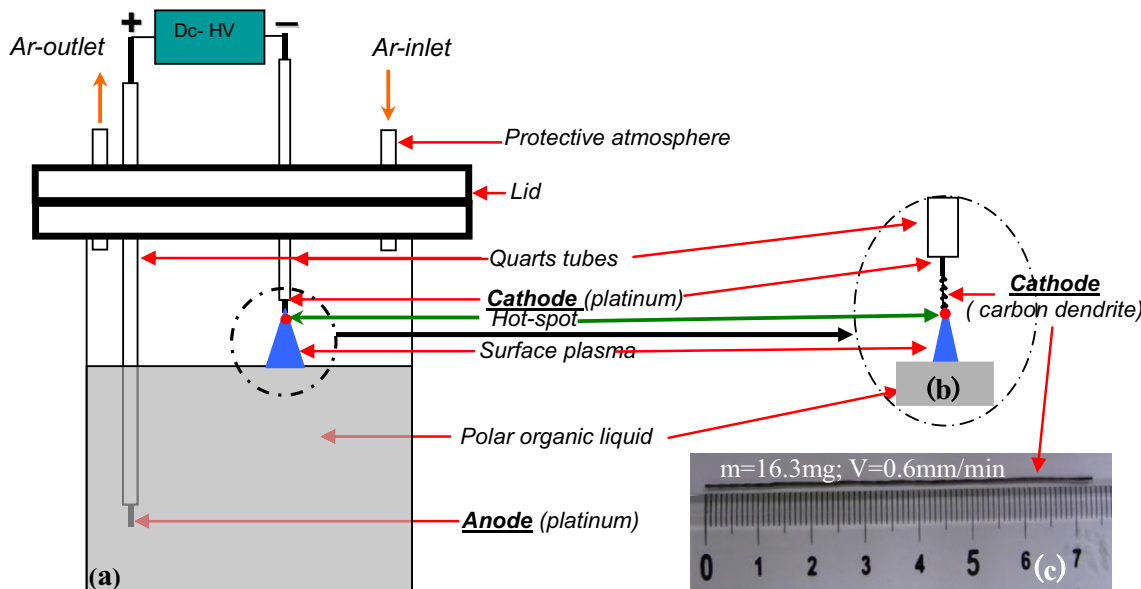


Fig. 1 – The general scheme of surface plasma process (a) and scheme of the carbon dendrite growth on the Pt-cathode (b). The final size of carbon dendrite (c). (A colour version of this figure can be viewed online.)

20 mm long portion of the carbon dendrite was hand milled in a ceramic vessel for the transmission electron microscope (TEM) investigations. We employed a TEM (Jeol JEM 3010EX) operating at 300 kV to characterize the internal structure of the carbon dendrite. An X-ray diffraction (XRD, Bruker AXS GmbH) analysis was carried out with monochromatic CuK α radiation and 0.9 kW X-ray power (30 kV, 30 mA). The carbon dendrite structure was characterized using a micro-Raman system (HORIBA Scientific, Japan) equipped with a 532-nm wavelength semiconducting laser.

3. Results and discussion

3.1. The mechanism of microplasma generation

Fig. 2(a) shows the voltage (V) and current (I) applied during the surface plasma process. The voltage and current have the pulsation about 33 kHz without a change of polarity. The values are $V = 0.6\text{--}1.1\text{ kV}$ and $I = 220\text{--}273\text{ mA}$, respectively (**Fig. 2**).

The mechanism of surface plasma generation is based the polarization of polar organic molecules under induction of external high electric field strength. Generally the surface plasma generation can be described as follows. The ethanol is a polar liquid with dielectric constant of $\epsilon = 25$, therefore, the ethanol molecules have a dipole moment even when the external the electric field is absent. The dipoles moment of ethanol molecules are maintained in both the liquid and gas phase. The dipoles are aligned with the direction of external electric field. Therefore, the electronic/dipole-relaxation polarization occurs in the liquid ethanol.

In the present experiment, the external electric field is non-uniform. The density of the dipoles was maximized in the cathode region located above the liquid ethanol surface. The dipole moments of the ethanol molecules were aligned with the external electric field in both the liquid phase and the gas phase mixture of Ar with C₂H₅OH. The maximum electric field strength occurred under the cathode, and the

electronic breakdown started between the cathode and the liquid ethanol surface. The ionization of Ar atoms and the decomposition of ethanol molecules were occurred due to the electronic breakdown and an electric current started to flow in the circuit. The decomposition of ethanol molecules, ionization of Ar atoms, and nucleation and growth of carbon dendrite occurred in the channel created by the surface plasma.

3.2. Growth mechanism of carbon dendrite

The carbon dendrite growth mechanism had two stages. The first stage of the surface plasma growth depended on the temperature of the organic liquid and the distance between Pt-cathode and ethanol surface. The plasma-induced decomposition of ethanol molecules had been previously studied before [15–17]. The second stage was characterized by the formation of a hot-spot and the growth of carbon dendrite (see **Fig. 1**). The carbon dendrite growth stabilized in 5–10 min after the surface plasma process started. The second stage of the growth defined the shape of the carbon dendrite.

One can assume that the carbon dendrite growth is a result of a carbon-cluster mechanism after the formation of the hot-spot in the second stage (**Fig. 3**). The plasma surface region presented in **Fig. 3** possibly corresponds to the formation and agglomeration of the carbon nanoclusters on the surface of the Pt/C-cathode. The plasma shaped determined the features of the outer surface of carbon dendrite during growth (see **Fig. 4**). The carbon dendrite growth occurred from top to bottom due to the plasma restriction of the surface (**Fig. 3**). Growth in the opposite direction was impossible.

3.3. Optical, SEM and TEM observations

Using the optical microscope we determined the carbon dendrite surface features over the carbon dendrite length of $l = 74\text{ mm}$ (**Fig. 1(c)**). **Fig. 4(a)** shows the carbon dendrite surface consisting of a great number of small nodular dendrites.

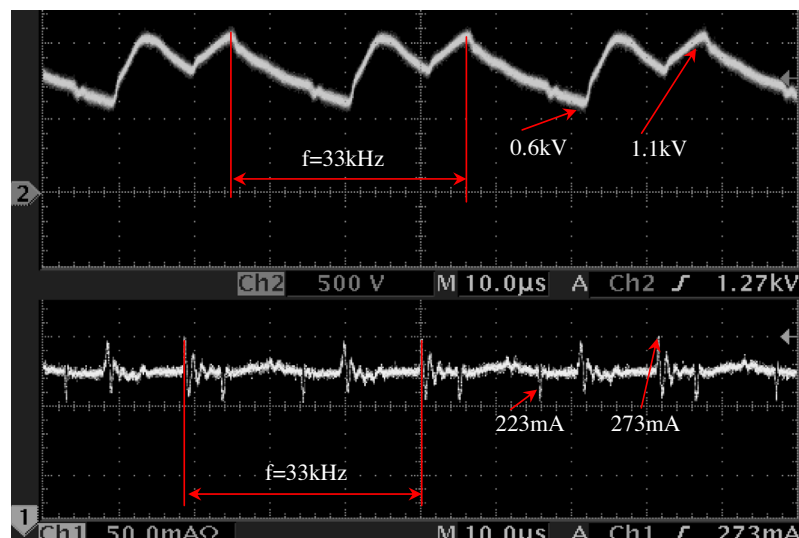


Fig. 2 – The oscilloscope recording of the voltage and current characteristics of surface plasma. (A colour version of this figure can be viewed online.)

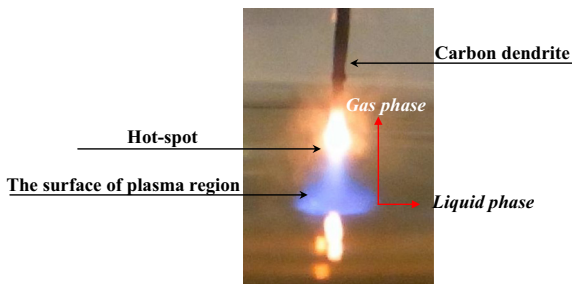


Fig. 3 – The photo-scheme of the second stage of carbon dendrite formation. (A colour version of this figure can be viewed online.)

Increasing the optical magnification allows us to determine that each nodule had a diameter of 5–10 µm as shown by arrows in Fig. 4(b). Therefore, each nodule consisted of the smaller nodules ranging from 2 to 5 µm in diameter (Fig. 4(c)). Further, these smaller nodules consisted of additional nodules, which had diameters less than 0.2–0.5 µm as shown by arrows in Fig. 4(d). Energy dispersive X-ray (EDX) analysis of the carbon nodules showed only two elements: carbon (97.09 Wt%) and oxygen (02.91 Wt%) (Fig. 4(c)). It should be mentioned that the carbon dendrite represents as cauliflower-like surface.

After mechanical milling of the carbon dendrite, we were able to estimate additional structure features (Fig. 5(a)). We assume that some of the part carbon dendrite was deformed, and the deformation looked like “flakes” as shown by arrows in Fig. 5(b). It was determined that the edge of the “flakes” consisted of carbon sheets as shown arrows in Fig. 5(c). Some carbon sheets had carbon layers up to 500 nm thick carbon layers (Fig. 5(d)).

High-resolution TEM (HR-TEM) observation of the carbon dendrite internal structure found carbon sheets consisting of layers. In the HR-TEM images, there were between 7 and 15 carbon layers in one carbon sheet as shown by arrows in Fig. 5(e) and (f). A large number of sheets have more than 15 layers. The HR-TEM observations (Fig. 5(e) and (f)) revealed that the carbon dendrite has a similar internal structure to that described by Harris [18], which includes a plurality of layers for glassy carbon.

The study of the fracture surface of carbon dendrite revealed its growth formation features (Fig. 6(a)–(c)). It was established that the carbon dendrite had two areas of crystals. The first central area consisted of equiaxial crystals as shown by arrows in Fig. 6(a). This area was about 230 µm in diameter (Fig. 6(c)). The equiaxial crystal size decreases near the center of the carbon dendrite as marked by arrows on the left side of Fig. 6(b). The second (peripheral) area was about 35 µm thick (Fig. 6(c)) and consisted of columnar crystals as shown by arrows on right side of Fig. 6(b).

The analysis of the carbon dendrite surface (where the hot-spot is formed) revealed the size and form of the equiaxial crystals. They were spherical crystals about 5–15 µm in diameter and consisted of a plurality of thickened carbon sheets marked by arrows on Fig. 6(d). It should be noted that the free space between the spherical crystals was filled up with the nodule-shaped crystals (Fig. 6(d)).

In Ref. [19], the carbon deposit growth within the arc patches was observed. Three stages were defined: nucleation, growth along the shortest path between the anode-graphite and cathode-graphite and growth in a direction subtending an angle to the shortest path between the anode-graphite and cathode-graphite. At a work gas pressure of $P = 30,000$ Pa, an H_2/CH_4 ratio of 90/10 and a discharge power of 36 W, the growth rate was 15 mm/h. The pyrocarbon

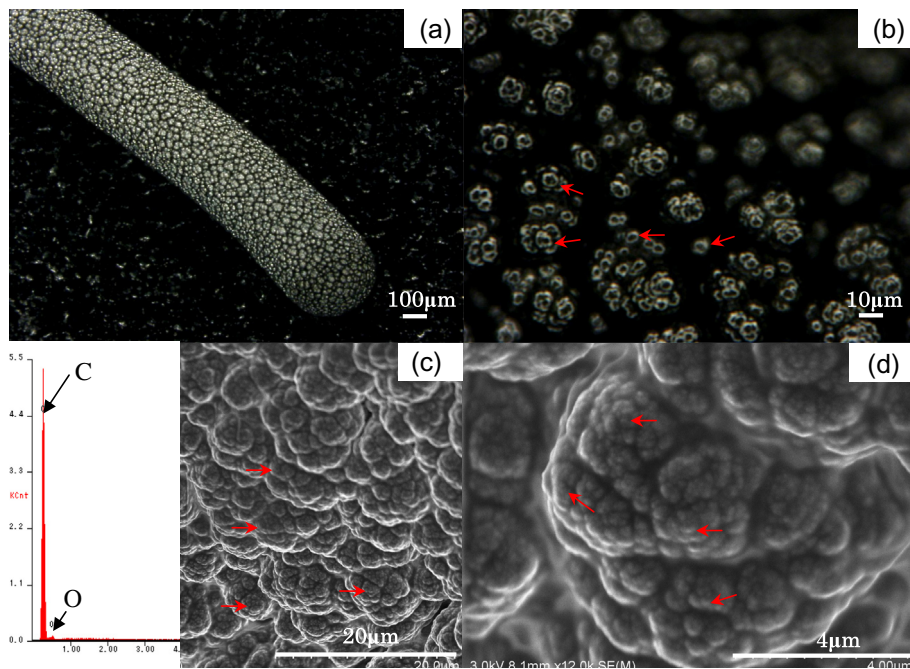


Fig. 4 – (a), (b) Optical and (c), (d) SEM images of the as-prepared cauliflower-like surface of carbon dendrite. (A colour version of this figure can be viewed online.)

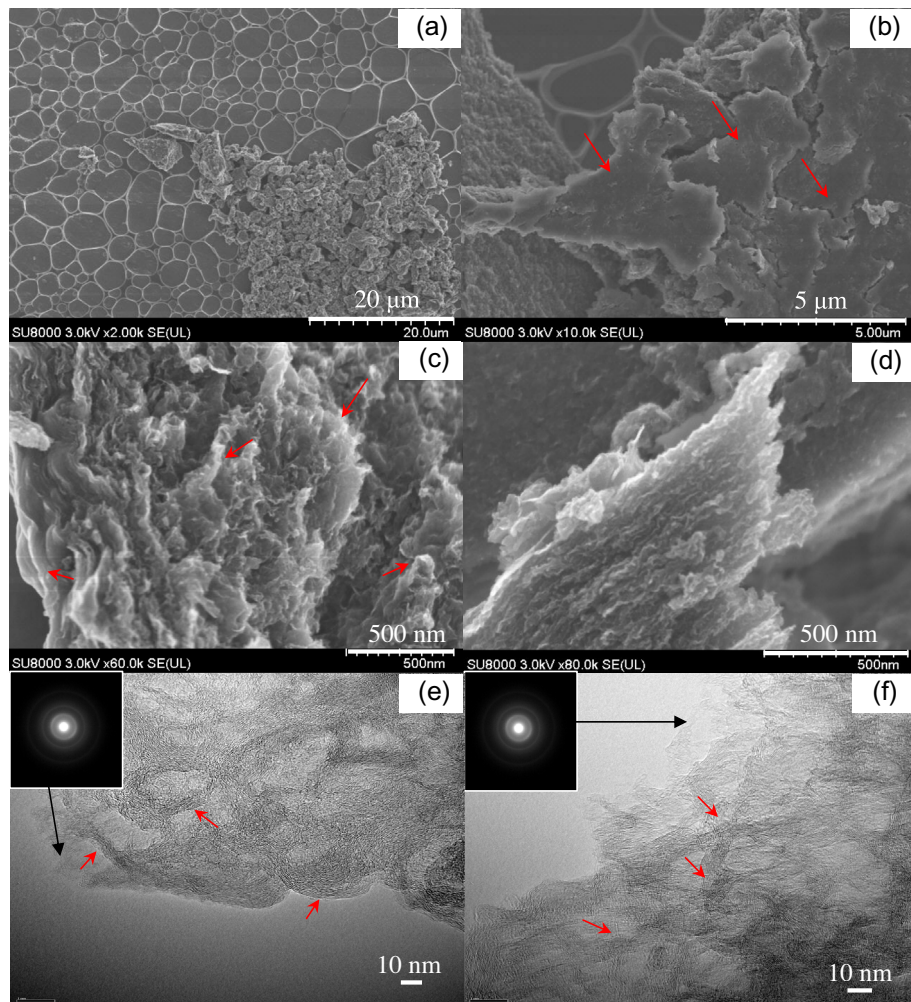


Fig. 5 – (a)–(d) SEM and (e) and (f) TEM images of carbon dendrite after mechanical milling. The inserts in (e) and (f) are electron diffraction patterns of the selected places of carbon dendrite. (A colour version of this figure can be viewed online.)

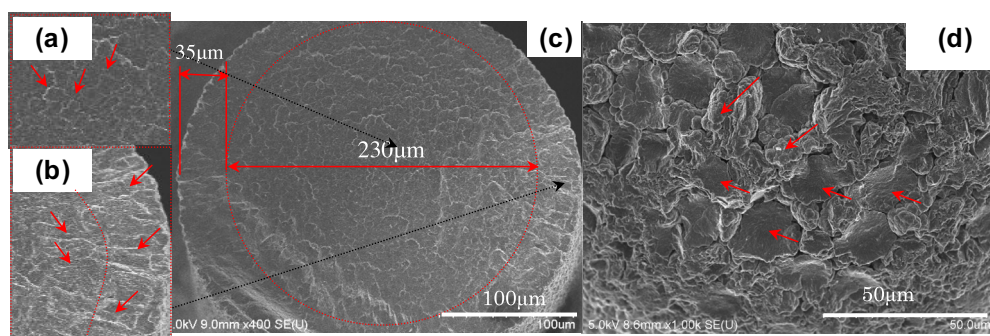


Fig. 6 – (a)–(c) SEM images of carbon dendrite fracture surface with central (a) and peripheral areas, respectively. (d) The carbon dendrite surface after of surface plasma process. (A colour version of this figure can be viewed online.)

diameter was about 3 mm. In accordance with the classification for carbon obtained during methane pyrolysis, the growth was considered to be “compact silver grey carbon” [19]. Koprinarov et al. did not discuss the external and internal of structure “compact silver grey carbon” so it was difficult to compare with our research.

If we assumed that ethanol pyrolysis occurred during our surface plasma process at temperature about 1000 °C, we must consider the growth mechanism for pyrocarbon. Bourrat et al. [20] classified three pyrocarbon growth mechanisms: rough laminar, regenerative laminar and dark laminar. Rough and regenerative laminar are anisotropic, while dark laminar is

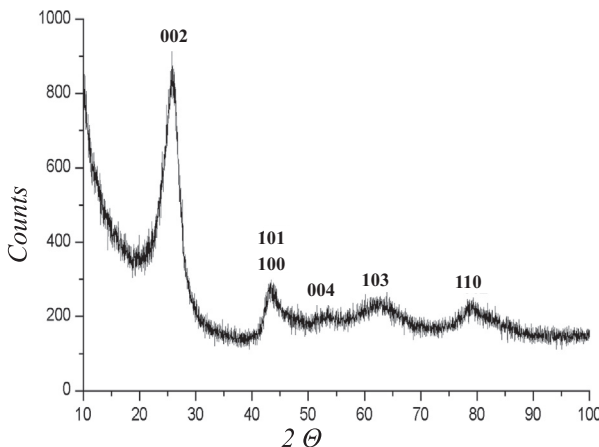


Fig. 7 – XRD profile of the as-prepared carbon dendrite about 20 mm long.

weakly anisotropic. Comparing our TEM images (Fig. 5(e) and (f)) with TEM image Ref. [20] revealed where the layer distortions formed Ω -like features in the texture (see arrows in Fig. 5(e) and (f)), corresponding to the growth dark laminar mechanism [20].

3.4. XRD analysis and Raman spectra of carbon dendrite

Fig. 7 shows the XRD pattern of the as-prepared carbon dendrite before mechanical milling. The XRD profile has several broad peaks over the $2\theta = 25.72^\circ$, $2\theta = 43.41^\circ$ and $2\theta = 78.49^\circ$ ranges which correspond to the interplanar carbon dendrite structure spacing of $d_{002} = 3.45$, $d_{101/100} = 2.08$ and $d_{110} = 1.228$, respectively. Other low intensity broad peaks over the $2\theta = 54.03^\circ$ and $2\theta = 65.03^\circ$ ranges correspond

to the interplanar spacings of $d_{004} = 1.69$ and $d_{103} = 1.43$, respectively (Fig. 7). Similar XRD patterns of glassy carbon films were observed by Heiman et al. [3].

It should be noted that the broad XRD peaks over the $2\theta = 25–26^\circ$, $2\theta = 43–44^\circ$ and $2\theta = 78–79^\circ$ were obtained for carbon aerosols particles in Ref. [5]. However, the carbon aerosols particles internal structure was disordered. These carbon aerosol particles were produced by non-thermal plasma-assisted decomposition of natural gas at near-ambient conditions [5].

Raman spectroscopy has been widely used to study the disorder, crystal formation, and bonding types in a variety of carbon materials. Large single-crystal graphite displays a single Raman peak at 1580 cm^{-1} (the G-peak) [3]. Microcrystalline carbon forms display an additional disorder-induced peak at 1350 cm^{-1} (the D-peak) [21]. The G- and D-Raman peaks of carbon dendrite were centered at approximately $1590–1600\text{ cm}^{-1}$ and $1344–1349\text{ cm}^{-1}$, respectively. The D-peak at $1344–1349\text{ cm}^{-1}$ is attributed to defects or structural disorder in the carbon dendrite. The G-peak position is sensitive to the particular graphitic carbon structure, varying from 1520 cm^{-1} for amorphous carbons to 1590 cm^{-1} for glassy carbon [24]. Fig. 8(a) shows the Raman spectra taken randomly at different points on the outer surface and Fig. 8(b) shows the Raman spectra taken across the carbon dendrite diameter (see Fig. 6(c)) with observation step of $20\text{ }\mu\text{m}$.

Changes in the relative intensities of the D- and G-peaks, as well as the peak positions and widths are sensitive to degree of disorder of the carbon structures. For example, Tuinstra and Koenig [26] were the first to show that the relative intensities of the D- and G-peaks $I_{1350\text{ cm}^{-1}}/I_{1600\text{ cm}^{-1}}$ are inversely proportional to the in-plane crystallite size (L_a). More recently, Knight and White [27] have collated data from the literature to confirm that this relationship holds for a wide range of sp^2 -bonded carbons over the range $25 < L_a < 3000$. Wopenka and et al., grouped the carbon grains into the different Raman types based on I_D/I_G intensity ratios as follows:

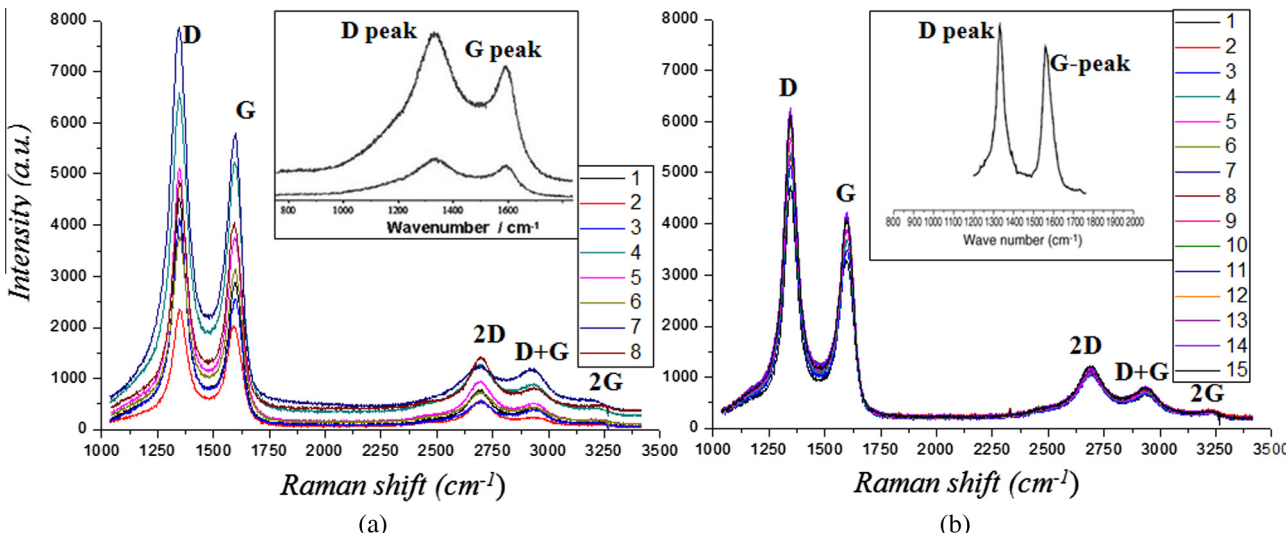


Fig. 8 – Raman spectra taken from the outer surface (a) and the cross-section (b) of the as-prepared carbon dendrite. Inserts show reference Raman spectrum of pyrocarbon [20] and glassy carbon film [24], respectively. (A colour version of this figure can be viewed online.)

well-ordered graphite ($I_D/I_G < 0.5$), disordered graphite ($0.5 < I_D/I_G < 1.1$), glassy carbon ($I_D/I_G > 1.1$) and unusual sp^2 -bonded graphitic carbon with extremely intense 2nd-order peaks relative to the 1st-order peaks [22,23].

The intensity ratio of D-to G-peaks (I_D/I_G) shows differences in the Raman spectra of the carbon dendrite outer surface and cross-section. The differences and scattering of I_D/I_G , depend on the crystals orientation on the outer surface and in the cross-section of the dendrite. On the one hand, the intensity ratio (I_D/I_G) had an average value of about 1.336 for the outer surface and about 1.470 for the cross-section. These values I_D/I_G correspond to glassy carbon structure [22,25]. On other hand, these values I_D/I_G had an average value of about 1.33–1.38 and correspond to pyrocarbon [20].

The second-order Raman spectra, over 2300 cm^{-1} , are even more sensitive to disorder and depend on heat treatment temperature [28]. The observed Raman bands at around $2680\text{--}2700\text{ cm}^{-1}$ (2D) and $3226\text{--}3239\text{ cm}^{-1}$ (2G) (Fig. 8) correspond to the allowed second harmonies of the vibrations at the D- and G-points in the first-order spectrum of graphite. The remaining band at around $2932\text{--}2936\text{ cm}^{-1}$ corresponds to the sum D and G-peaks.

4. Conclusions

The newly developed method presented in this paper allows growth of carbon dendrites that exhibit glassy carbon- and pyrocarbon-like structures, by using surface plasma on the cathode surface above dehydrated ethanol. This process is based on the polarization of polar organic molecules under the influence of a very strong external electric field.

The outer surface of a carbon dendrite consists of multiple carbon nodules $5\text{--}10\text{ }\mu\text{m}$ in diameter. Each nodule consists of smaller nodules $2\text{--}5\text{ }\mu\text{m}$ in diameter. These smaller nodules consist of additional nodules, which are less than $0.2\text{--}0.5\text{ }\mu\text{m}$ in diameter.

Raman spectral analysis revealed the glassy carbon- and/or pyrocarbon-like internal structure of the carbon dendrites with I_D/I_G ranging from 1.336 to 1.470. The dendrite growth mechanism involved two stages: (1) crystal formation on the nucleating surface of the Pt-cathode, and (2) appearance of a hot-spot and top-to-bottom carbon dendrite growth.

By varying the experimental conditions, the internal and external structures of carbon dendrites could be modified for different application (e.g., catalyst, battery electrodes, modifier for foundry of ferrous metallurgy, reinforcement for aluminum and copper alloys, etc.). Another advantage of the plasma surface process is that it enables growth of carbon dendrite on dielectric surfaces without increasing of plasma power generation.

Acknowledgment

This work was supported by Nano-macro materials, devices and system research alliance. The authors would like to acknowledge Prof. Takaaki Tomai of Tohoku University for his helpful discussion on Raman spectrum measurements.

REFERENCES

- [1] Suzuki T, Wada S, Suzuki M, Yamazaki T, Noma T. Diamond deposition by DC plasma above the liquid surface of the water-methanol and water-ethanol systems. *J Mater Sci Lett* 2000;19:1899–901.
- [2] Suzuki T, Tsukada M, Yamazaki T, Wada S, Noma T. Process parameters for diamond synthesis assisted by DC plasma using a water-ethylene glycol solution. *J Mater Sci* 1999;34:4761–5.
- [3] Heiman A, Lakin E, Zolotovskaya E, Hoffman A. Microstructure and stress in nano-crystalline diamond films deposited by DC glow discharge CVD. *Diamond Relat Mater* 2002;11:601–7.
- [4] Gouzman I, Shima-Edelstein R, Comtet G, et al. Influence of substrate nature on the d.c.-glow discharge induced nucleation of diamond. *Diamond Relat Mater* 1999;8:132–8.
- [5] Muradova N, Smitha F, Bockerman G, Scammon K. Thermocatalytic decomposition of natural gas over plasma-generated carbon aerosols for sustainable production of hydrogen and carbon. *Appl Catal A: General* 2009;365:292–300.
- [6] Hunga Tsung-Chi, Chenb Chia-Fu, Chenc Chien-Chung, Whang Wha-Tzong. Catalyst-free, low-temperature growth of high-surface area carbon nanoflakes on carbon cloth. *Appl Surf Sci* 2009;255:3676–81.
- [7] Bo Zheng, Kehan Yu, Ganhu Lu, Shumao Cui, Mao Shun, Junhong Chen. Vertically oriented graphene sheets grown on metallic wires for greener corona discharges: lower power consumption and minimized ozone emission. *Energy Environ Sci* 2011;4:2525.
- [8] Bo Zheng, Kehan Yu, Ganhu Lu, Wang Pengxiang, Mao Shun, Junhong Chen. Understanding growth of carbon nanowalls at atmospheric pressure using normal glow discharge plasma-enhanced chemical vapor deposition. *Carbon* 2011;49:1849–58.
- [9] Yihong Wu, Qiao Peiwen, Chong Towchong, Shen Zexiang. Carbon nanowalls grown by microwave plasma enhanced chemical vapor deposition. *Adv Mater* 2002;14(1):64–7.
- [10] Chen Qiang, Kaneko Toshiro, Hatakeyama Rikizo. Characterization of pulse-driven gas-liquid interfacial discharge plasmas and application to synthesis of gold nanoparticle-DNA encapsulated carbon nanotubes. *Curr App Phys* 2011;11:S63–6.
- [11] Chiang Wei-Hung, Richmonds Carolyn, Mohan Sankaran R. Continuous-flow, atmospheric-pressure microplasmas: a versatile source for metal nanoparticle synthesis in the gas or liquid phase. *Plasma Sources Sci Technol* 2010;19:1–8.
- [12] Kaneko T, Baba K, Hatakeyama R. Liquid-gas interfacial plasmas for the formation of novel nanobiomaterials. *Plasma Fusion Res* 2009;4:028–1–8.
- [13] Bruggeman Peter, Liu Jingjing, Degroote Joris, Kong Michael G, Vierendeels Jan, Leys Christophe. Dc excited glow discharges in atmospheric pressure air in pin-to-water electrode systems. *J Phys D: Appl Phys* 2008;41:1–11.
- [14] Kaneko T, Baba K, Hatakeyama R. Gas-liquid interfacial plasmas: basic properties and applications to nanomaterial synthesis. *Plasma Phys Control Fusion* 2009;51:1–8.
- [15] Yanguas-Gil A, Hueso JL, Cotrino J, Caballero A, González-Eliepa AR. Reforming of ethanol in a microwave surface-wave plasma discharge. *Appl Phys Lett* 2004;85(18):4004–6.
- [16] Vessellil E, Coslovich G, Comelli G, Rosei R. Modelling of ethanol decomposition on Pt(111): a comparison with experiment and density functional theory. *J Phys: Condens Matter* 2005;17:6139–48.
- [17] Levko D, Tsymbalyuk A, Shchedrin AI. Plasma kinetics of ethanol conversion in a glow discharge. *Plasma Phys Repor* 2012;38(11):913–21.

- [18] Harris PJF. Fullerene-related structure of commercial glassy carbons. *Phil Mag* 2004;84(29):3159–67.
- [19] Koprinarov N, Konstantinova M, Pchelarov G. Growth of plasma pyrolytic carbon. *Carbon* 1994;32(4):559–62.
- [20] Bourrat X, Langlais F, Chollon G, Vignoles GL. Low temperature pyrocarbons: a review. *J Braz Chem Soc* 2006;17(6):1090–5.
- [21] Reich S, Thomsen C. Raman spectroscopy of graphite. *Phil Trans R Soc Lond A* 2004;362:2271–88.
- [22] Wopenka B, Xub YC, Zinner E, Amari S. Murchison presolar carbon grains of different density fractions: a Raman spectroscopic perspective. *Geochimica et Cosmochimica Acta* 2013;106:463–89.
- [23] Li K, Zhang D, Guo L, Li H. Micro- and nano-structure characterization of isotropic pyrocarbon obtained via chemical vapor deposition in hot wall reactor. *J Mater Sci Technol* 2010;26(12):1133–8.
- [24] Prawer S, Ninio F, Blanchonette I. Raman spectroscopic investigation of ion-beam-irradiated glassy carbon. *J Appl Phys* 1990;68:2361–6.
- [25] Chu Paul K, Li Liuhe. Characterization of amorphous and nanocrystalline carbon films. *Mater Chem and Phys* 2006;96:253–77.
- [26] Tuinstra F, Koenig JL, Raman J. Spectrum of graphite. *Chem Phys* 1970;53:1126–30.
- [27] Knight DS, White WB. Characterization of diamond films by Raman spectroscopy. *J Mater Res* 1989;4:385–93.
- [28] Soukup L, Gregora I, Jastrabik L, et al. Raman spectra and electrical conductivity of glassy carbon. *Mater Sci Eng B* 1992;11:355–7.